



An innovative approach to measuring hygroscopic light scattering enhancement using a humidified single-nephelometer system

Lenka Suchánková^{1,2,3}, Jakub Ondráček¹, Naděžda Zíková¹, Petr Roztočil¹, Petr Vodička¹, Roman Prokeš^{2,3}, Ivan Holoubek^{2,3+}, Vladimír Ždímal¹

¹Institute of Chemical Process Fundamentals of the Czech Academy of Sciences, Prague, 165 00, Czech Republic

²Global Change Research Institute of the Czech Academy of Sciences, Brno, 603 00, Czech Republic

³RECETOX, Faculty of Science, Masaryk University, Brno, 611 37, Czech Republic

⁺ deceased

Correspondence to: Lenka Suchánková (suchankova@icpf.cas.cz)

Keywords: aerosol light scattering properties, hygroscopicity, suburban environment, climate change

Abstract: Most atmospheric aerosol particles are hygroscopic, meaning they absorb water from the surrounding air, altering their size, shape, overall chemistry, refractive index, and thus light-scattering properties — an effect with important implications for Earth's radiative balance. The scattering enhancement factor, $f(RH)$, and backscattering enhancement factor, $f(RH)_{bsp}$, quantify the increase in light scattering under elevated relative humidity (RH). These parameters are typically measured using two nephelometers operating under dry ($RH < 40\%$) and humidified ($RH > 80\%$) conditions, a method prone to inter-instrument uncertainties. This study presents a novel single-nephelometer system that reduces measurement uncertainty and studies aerosol hygroscopic behavior in the inadequately represented European urban environment. The system was deployed at a suburban site in Prague, Suchdol, Czech Republic, from November 2022 to August 2023. Results revealed low aerosol hygroscopicity, likely due to a well-mixed aerosol population dominated by black and brown carbon. Both enhancement factors peaked in spring, possibly influenced by favorable conditions for new particle formation and changes in aerosol composition, size distribution, and meteorological conditions. In contrast, low values in summer reflected a composition shift toward black carbon-dominated aerosols from traffic emissions, with particle growth being disrupted, potentially due to the structural compaction of black carbon aggregates under high RH. While $f(RH)$ and $f(RH)_{bsp}$ generally increased with decreasing concentrations of light-absorbing particles, organic carbon, particularly its most volatile fractions, significantly enhanced aerosol hygroscopicity in the urban environment. Despite low aerosol hygroscopicity, increased RH significantly influenced aerosol climate-relevant variables.

1. Introduction

Atmospheric aerosols play a critical role in the Earth's energy budget through direct aerosol-radiation interactions (ARI) by the scattering and absorption of short- and long-wave radiation and indirect aerosol-cloud interactions (ACI) by changes in the microphysical and radiative properties of clouds, respectively (Boucher, 2015; IPCC, 2021). The Sixth Assessment Report of the IPCC estimated the total aerosol effective radiative forcing (ERF) to be -1.1 [-1.7 to -0.4] $W\ m^{-2}$ over 1750–2019 (Foster et al., 2023). Despite growing research on the aerosol radiative effects (e.g., Toll et al., 2019; Williams et al., 2022; Zhang et al., 2025 and references herein), aerosol ERF remains the most significant uncertainty in climate models due to the high spatial and temporal variability of aerosol properties, limited understanding of pre-industrial aerosol conditions, and the indirect aerosol-induced changes in the atmosphere (Carslaw et al., 2017; Kahn et al., 2023; Watson-Parris and Smith, 2022).

Hygroscopicity, defined as the ability of aerosol particles to attract and absorb moisture from the surrounding environment, critically alters particle size, shape, and refractive index (Burgos et al., 2019; Titos et al., 2021) and impacts the angular distribution of scattered light and thus aerosol optical properties (Fierz-Schmidhauser et al., 2010; Zieger et al., 2015).



40 Since the globally measured long-term in situ aerosol measurements are standardized below 40 % relative humidity (RH)
 41 (WMO/GAW, 2016), these "dry" conditions do not reflect the real atmosphere, leading to an inadequate understanding of
 42 aerosol water uptake, which contributes to significant uncertainties affecting aerosol climate effects (Burgos et al., 2020; Myhre
 43 et al., 2013; Ray et al., 2024).

44 The light scattering enhancement due to humidity can be expressed by the light scattering enhancement factor $f(RH)$
 45 as in Eq. (1):

$$46 \quad f(RH) = \frac{\sigma_{sp}(RH, \lambda)}{\sigma_{sp}(RH_{dry}, \lambda)}, \quad (1)$$

47 where $\sigma_{sp}(RH, \lambda)$ and $\sigma_{sp}(RH_{dry}, \lambda)$ denote total scattering coefficients under elevated RH conditions and dry conditions
 48 measured at the same wavelength λ , respectively (Covert et al., 1972). A similar formulation applies for backscattering,
 49 $f(RH)_{bsp}$ (Titos et al., 2021).

50 Several approaches to investigate $f(RH)$ have been proposed. Tandem-humidified nephelometer systems occurred in the
 51 1960s and have undergone substantial innovations since then (Pilat and Charlson, 1966). These systems consist of one
 52 nephelometer measuring under dry conditions and a second nephelometer measuring a humidified aerosol sample. Two main
 53 instrumental set-ups were identified in the 26 tandem-humidified nephelometer measurements from ground-based sites
 54 worldwide (Burgos et al., 2019). The "NOAA design" directs aerosol through a first dry and later humidified nephelometer
 55 (e.g., Doherty, 2005; Liu and Li, 2018), while the "PSI design" splits the aerosol into parallel dry and humidified paths (e.g.,
 56 Zieger et al., 2015, 2014). Both systems used an RH scanning regime (20 to 95 % RH) for the humidified nephelometer (Titos
 57 et al., 2016).

58 The comparison of the integrating nephelometer TSI 3563 with AURORA 3000 possessed an overall uncertainty of 2-5 %
 59 for σ_{sp} and 3-11 % for σ_{bsp} in laboratory conditions, respectively (Müller et al., 2011). The experimental set-ups comprising
 60 two or more instruments could introduce additional uncertainty to the resulting data, considering different sampling lines for
 61 nephelometers, non-symmetrical apparatus, or the critical measurement part under highly humid conditions (Anderson et al.,
 62 1996).

63 Thus, this study introduces a novel single-nephelometer system to reduce additional uncertainties in the $f(RH)$ estimation
 64 and investigates ambient aerosol particles' light scattering hygroscopic behavior at the suburban site. To the best of our
 65 knowledge, only one study of aerosol hygroscopic behavior in a suburban/urban European environment was published (Titos
 66 et al., 2014). This study provides a unique insight into light scattering enhancement in European urban/suburban environments.

67 2. Materials and Methods

68 2.1. Description of the site

69 The instrumentation set-up was developed and tested at the Institute of Chemical Process Fundamentals (ICPF) of the
 70 Czech Academy of Sciences in Prague, Czech Republic. The ICPF also runs a Suchbátka atmospheric station located on the
 71 institute campus (50° 7' 35" N, 14° 23' 5" E, 277 m a.s.l., Figure 1). The station is a suburban site and an Aerosol In Situ
 72 National Facility (AIS NF) of the ACTRIS ERIC (Aerosols, Clouds, and Trace gases Research InfraStructure, European
 73 Research Infrastructure Consortium; <https://www.actris.net/>). The aerosol instruments are positioned within the sampling
 74 container, with the sampling heads situated approximately 4 meters above the ground.

75 The station is located at the periphery of the plateau above the capital, Prague (1.37 million citizens in 2025), 5 km from
 76 the city center. The site is surrounded by residential housing, utilizing gas as the primary energy source for heating (80 %),
 77 while the remainder utilizes electricity (16 %), community heating (2 %), or burns solid and liquid fuels (less than 2 %) (Český
 78 statistický úřad, 2021). The nearest road is situated at a distance of 250 m (10,000-15,000 cars per day, Vodička et al., 2013),
 79 but no major road is located within 1 km of the site. The Václav Havel airport is situated 9 km SW of the site. The agricultural



80 fields are located within a 2 km radius to the west. The predominant wind direction at the site is from the WSW (mainly
 81 summer and winter), with a notable influence of SE during winter and NW during spring (Fig. S.1). The measurement
 82 campaign was conducted from 15 November 2022, to 19 August 2023.

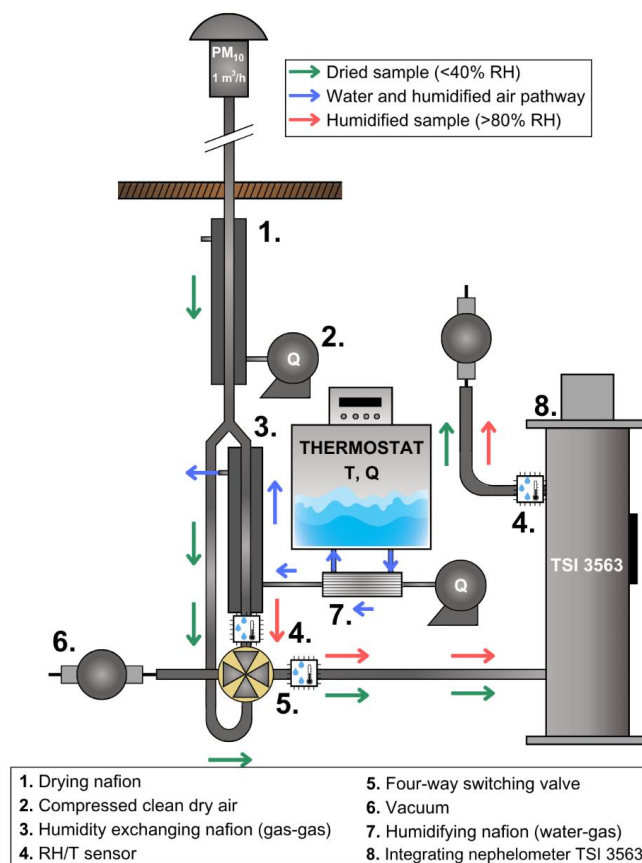


83

84 **Figure 1: Location of Suchdol ACTRIS ERIC AIS NF site within Prague, Czech Republic. Map source: © Seznam.cz, a.s.**

85 2.2. The single-nephelometer instrumentation

86 Aerosol particles were sampled through a PM₁₀ sampling head (Leckel, GmbH) and subsequently dried by a custom-built
 87 Nafion dryer (Permapure) to achieve the RH level below 40 % (Figure 2, No. 1). The total aerosol flow of 10 lpm was divided
 88 equally between two parallel sampling lines: a dry sampling line (5 lpm) and a humidified sampling line (5 lpm). The dry
 89 sample was passed through the sampling system to the integrating nephelometer (TSI 3563) without additional adjustments.
 90 The other line led to the second Nafion membrane, functioning as a water exchange medium, facilitating counter-current mass
 91 transfer between humidified particle-free air and the aerosol sample (Figure 2, No. 3). This humidification process aimed to
 92 achieve a sample RH \geq 80 %.



93

94 **Figure 2: A design of the single-nephelometer set-up system for studying aerosol hygroscopic behavior.**

95 Humid particle-free air was produced in the closed circulation system (Figure 2, blue arrows). Demineralized water,
 96 heated in a controlled manner by the thermostat, was directed to the bundle Nafion membrane (Figure 2, No. 7), where mass
 97 transfer between water (in channels) and the dry particle-free air (outside the channels) occurred. The excessive water was
 98 later returned to the thermostat, and the humid particle-free air flowed into the humidity-exchanging Nafion membrane (Figure
 99 2, No. 3). The temperature of the demineralized water and the flow rate of the humid particle-free air were regulated to achieve
 100 the desired RH level in the humidity-exchanging Nafion. An RH/T sensor (HYT939, Innovative Sensor Technology, AG) was
 101 installed before the switching valve to control the RH in the humidified sample. Since the RH sensor inside the measurement
 102 cell was not sufficiently accurate, additional RH/T sensors were positioned immediately in front of the inlet and after the outlet
 103 of the instrument (Figure 2, No. 4) to control the RH dynamics and to calculate the dew point temperature T_{dew} , which was
 104 used to estimate the real RH of the sample (see Chapter 2.4 Data treatment). All RH/T sensors were calibrated against a
 105 standard thermometer (F250 MKII, Automatic System Laboratories) and a dew point mirror (CMH2, Alpha Moisture Systems)
 106 at the beginning of the campaign.

107 Every 60 minutes, the four-way switching valve (Figure 2, No. 5) automatically directed either the dry or the
 108 humidified sample to the TSI 3563 integrating nephelometer (Figure 2, No. 8). First, a 10-minute conditioning period was
 109 initiated to reach the target RH of the sample, followed by a 50-minute measurement period as determined and optimized by
 110 pilot testing. During the dry sample measurement, the automatic switching valve allowed the dry sample to flow directly to



the nephelometer, and the humidified sample was directed to the exhaust (Figure 2, No. 6). And vice versa, when the humidified aerosol sample was sampled to the nephelometer, the dry sample was discarded.

The thermostat temperature and the flow rate of the humidified particle-free air were checked regularly to ensure proper humidification of the sample and to prevent condensation inside the instrument. All parts sensitive to changes in RH (humidity-exchanging Nafion, tubing within the closed humidity circuit, and inlet tubing to the nephelometer) were insulated to prevent heat losses and water condensation.

Upon reaching the nephelometer measuring cell, a dry or humidified aerosol sample was illuminated with a halogen lamp at an angle range of 7° – 170° . The scattered light passed through three band-pass filters and was detected in photomultiplier tubes (PMT) at 450, 550, and 700 nm wavelengths. The resulting total scattering and backscattering coefficients (σ_{sp} and σ_{bsp}) with a time resolution of 1 minute.

The nephelometer was calibrated twice a day with particle-free air and fully calibrated every 2–3 months with CO_2 as the high-span gas and particle-free air as the low-span gas, always in the dry measurement regime. The continuous dry measurement was performed approximately once a month (overnight) to avoid water condensation inside the instrument.

However, it should be stated that such a measurement approach possesses the limitation of reduced time resolution and a lack of parallel measurement of dry and wet aerosol properties, important for humidogram analyses.

2.3. Auxiliary measurements

The Mobility Particle Size Spectrometer (MPSS) measured the aerosol particle number concentration with a time resolution of 5 minutes, using a custom-built Differential Mobility Analyzer (DMA, both TROPOS, Germany), positive high-voltage power supply, and Condensational Particle Counter (CPC 3772, TSI). The MPSS ranged from 10 to 800 nm, 32 size channels per decade, with data further subdivided into size modes: 8–100 nm, 100–200 nm, 200–500 nm, and particles above 500 nm for the analysis. An additional total count CPC (3750, TSI) measured the total particle number concentration of particles larger with $d_p(50)$ at 10 nm.

Elemental and organic carbon (EC and OC) concentrations were measured from November 2022 to July 2023 using a semi-online field analyzer from Sunset Laboratory Inc. (USA) (Bauer et al., 2009). The analyzer was connected to a PM_{10} (November – December 2022) and $\text{PM}_{2.5}$ (rest of the period) inlet with a flow rate of 8 lpm. Samples were collected at 2-hour intervals on a quartz fiber filter and analyzed according to the shortened EUSAAR2 protocol (Cavalli et al., 2010). Each measurement was corrected for charring, and the RTCalc726 software automatically determined the split point between EC and OC using a linear fit of laser and temperature corrections. OC was divided into fractions based on temperature. The most volatile fractions, OC1 and OC2, volatilize at 200 °C and 300 °C and are commonly present in fresh vehicle exhaust, biomass burning, and coal combustion (Shen et al., 2025; Vodička et al., 2015). OC3 and OC4 subfractions volatilize at 450 °C and 650 °C and represent less volatile fractions of OC with higher molecular weights and are associated with chemical aging and the products of photochemical reactions (Aswini et al., 2019; Shen et al., 2025). The instrument was equipped with a parallel carbon plate denuder to eliminate volatile organic compounds and prevent positive bias in OC measurements. Instrument blanks were recorded daily at midnight.

A multiwavelength aethalometer (Model AE33, Magee Scientific, USA, 2018) continuously measured light absorption by particles at seven wavelengths (370, 470, 520, 590, 660, 880, and 950 nm). Particles were sampled through the PM_{10} sampling head (Leckel GmbH) at a flow rate of 5 lpm, dried in a custom-made Nafion dryer (TROPOS, Leipzig, Germany), and deposited onto tetrafluoroethylene (TFE) coated glass filter tape. Light transmission through the deposited sample is measured and compared to the blank filter tape spot as a reference, resulting in absorption coefficient (σ_{ap} , Mm^{-1}) and equivalent black carbon concentration (eBC, $\mu\text{g m}^{-3}$) data.



151 Ambient temperature (T), RH, wind speed (WS), wind direction (WD), global solar radiation (GLRD), and ozone (O₃)
 152 concentration were measured hourly in the Czech Hydrometeorological Institute container located next to the ACTRIS AIS
 153 container with all the aerosol instruments.

154 2.4. Data treatment

155 2.4.1. Humidified nephelometer system

156 Four subsystems working simultaneously were needed to obtain valid datasets from the measurements: nephelometer
 157 measurement, automatic switching between dry and humid measurements, humidification of the sample, and RH/T sensors.

158 The TSI 3563 integrating nephelometer data set was processed according to the EMEP Standard Operating Procedure.
 159 The raw σ_{sp} and σ_{bsp} data at all wavelengths were validated (removal of invalid, missing, and calibration data). Values below
 160 the limit of detection (LOD) were replaced by LOD/2 values, corrected to a non-Lambertian illumination according to
 161 Anderson and Ogren (1998), and standardized to STP conditions (273.15 K, 1013.25 hPa).

162 The automatic four-way switching valve was controlled using a custom-made LabVIEW program. The resulting data
 163 set was paired with the nephelometer data set to identify dry and humidified measurements.

164 All datasets produced by the RH/T sensors regulating the thermostat temperature and the flow of humidified particle-free air
 165 to achieve the desired RH of the sample were also recorded using a custom-made LabVIEW program.

166 Temperature and RH data from all three sensors were corrected using calibration curves derived from comparing with
 167 the referenced thermometer and the dew point mirror. The real RH of the sample was derived by assuming that the dew point
 168 temperatures in front of and behind the cell are similar (Ren et al., 2021). The approximated Magnus-Tetens formula (Alduchov
 169 and Eskridge, 1997) was used to calculate the dew point temperatures of both RH/T and from the mean T_{dew} , the saturation
 170 vapor pressure, p_{sat} , at T_{dew} was calculated as in Eq. (2):

$$171 \quad p_{sat} = a * e^{\frac{b * T_{dew}}{T_{dew} + c}}, \quad (2)$$

172 where a, b, and c are empirical constants derived from the experimental data: a = 6.112 hPa, b = 17.67, and c = 243.51 (b and
 173 c are dimensionless); T_{dew} in °C.

174 A similar approach was used to calculate the saturation vapor pressure at the temperature in the measuring cell, T_{cell} — p_{cell} .

175 The final RH of the sample in the measuring cell, RH_{cell} , was calculated as follows in Eq. (3):

$$176 \quad RH_{cell} = \left(\frac{p_{sat}}{p_{cell}} \right) * 100. \quad (3)$$

177 The RH_{cell} data set was later combined with the nephelometer and switching valve data. RH_{cell} with valve position variables
 178 was used to separate the data into dry ($RH \leq 40\%$) and humidified ($RH \geq 80\%$) datasets, with data corresponding to the range
 179 of $40\% < RH < 80\%$ being discarded. The dry and humidified datasets were averaged every hour.

180 The enhancement factors $f(RH)$ and $f(RH)_{bsp}$ were calculated to obtain information about light scattering enhancement
 181 due to hygroscopicity. In this study, $f(RH)$ was calculated based on "humid-centered" and "dry-centered" intervals to avoid the
 182 influence of possible extreme pollution events at the site (Fig. 3). The humid-centered interval was calculated by dividing the
 183 average humidified σ_{sp} value by the mean of two lateral 1-hour averaged dry σ_{sp} (Fig. 3, gray). The dry-centered interval was
 184 calculated by dividing the average of two lateral 1-hour averaged humidified σ_{sp} by the 1-hour averaged dry σ_{sp} value (Fig. 3,
 185 ochre). Extreme and invalid values were inspected and discarded if necessary. The data coverage of the entire measurement
 186 campaign, including individual seasons, as well as the variability of RH and temperature under humid and dry conditions, can
 187 be found in Table S.1, Table S.2, and Fig. S.1 in Supplementary Materials.

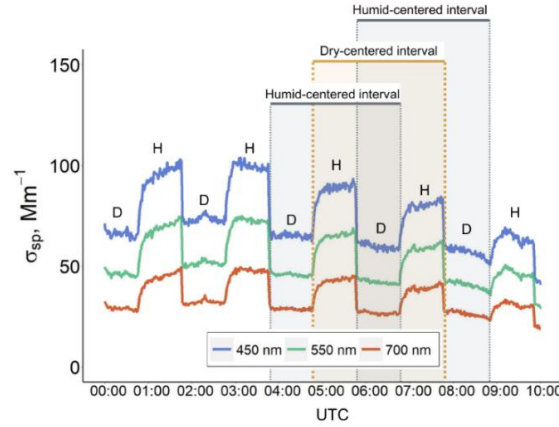


Figure 3: The example of $f(RH)$ calculation from a single-nephelometer measurement on December 12, 2022. The D and H symbols indicate "dry" and "humid" measuring intervals of σ_{sp} .

2.4.2. Relationship between aerosol scattering and absorption

To describe the spectral dependence of light scattering, the Scattering Ångström Exponent SAE was calculated as (Clarke and Kapustin, 2010):

$$SAE_{\lambda_1-\lambda_2} = -\frac{\log\left(\frac{\sigma_{sp}(\lambda_1)}{\sigma_{sp}(\lambda_2)}\right)}{\log\left(\frac{\lambda_1}{\lambda_2}\right)}, \quad (4)$$

where λ_1 and λ_2 are the wavelengths of light at which σ_{sp} was measured. SAE contains information about aerosol size: SAE values < 1 indicate the predominance of particles in the coarse mode, while SAE values ≥ 2 indicate a predominance of the aerosol fine mode (Seinfeld and Pandis, 2006).

In addition to SAE, ΔSAE was defined (Perrone et al., 2018) in Eq. (5):

$$\Delta SAE = SAE_{450-550} - SAE_{550-700}, \quad (5)$$

and provides insight into the relative contribution of fine and coarse mode particles and whether the particle size distribution is mono-, bi-, or multimodal. Positive ΔSAE values indicate the presence of two distinct modes—a fine mode and a coarser one—while negative ΔSAE values suggest the dominance of a single fine particle mode (Perrone et al., 2018).

The Absorption Ångström Exponent (AAE), which describes a spectral dependence of light absorption, was calculated analogously from σ_{ap} (Mbengue et al., 2021). AAE can provide information on chemical composition: AAE values < 1 could indicate BC core or non-absorbing coating particles, AAE values around 1 are classified as BC aerosol, while AAE values around 2 and higher indicate light absorption in ultraviolet and blue spectral regions, suggesting the presence of organic carbon — brown carbon BrC in this study — or mineral dust (Cappa et al., 2016).

To estimate the dominant aerosol type at the site, we used the AAE vs. SAE plot from Cappa et al. (2016), which can estimate the potential aerosol type without direct information on the chemical composition. For the aerosol type assessment in this study, the AAE was calculated at 520–660 nm and the SAE at 450–550 nm. The AAE vs. SAE plots were additionally color-coded with the Single Scattering Albedo (SSA), the ratio of the aerosol light scattering, and the total aerosol light extinction (light scattering plus absorption) at the predefined wavelength λ defined in Eq. (6):

$$SSA_{\lambda} = \frac{\sigma_{sp}(\lambda)}{\sigma_{sp}(\lambda) + \sigma_{ap}(\lambda)}. \quad (6)$$



214 Sites predominantly influenced by aerosol scattering (clean marine or remote Arctic sites) exhibit SSA values close to 1, while
 215 anthropogenically influenced sites exhibit significantly lower SSA (Pandolfi et al., 2018). In this study, also the humidified
 216 equivalent of SSA was calculated from dry measurements of σ_{ap} (RH < 40 %) and humidified σ_{sp} (RH > 80 %).

217 The asymmetry factor g describes the angular distribution of the scattered light and is defined as the average cosine
 218 of the angle between the incident light and the scattered beam θ , weighted by the probability of scattering for each possible
 219 angle. Based on the Henyey-Greenstein approximation (Andrews et al., 2006; Wiscombe and Grams, 1976):

$$220 \quad g_{\lambda} = -7.143889b_{\lambda}^3 + 7.464439b_{\lambda}^2 - 3.96356b_{\lambda} + 0.9893, \quad (7)$$

221 where b is the hemispheric backscattering ratio. g ranged from -1 for completely back-scattered light to 1 for completely
 222 forward-scattered light and is one of the essential inputs for the radiative transfer models.

223 The hemispheric backscattering ratio b denotes the fraction of light scattered back to the upper hemisphere of the
 224 particle and the total scattered light and can be measured directly from the optical instrument without knowledge of the
 225 scattering phase function (ranging from 0 to 1) calculated following Eq. (8):

$$226 \quad b_{\lambda} = \frac{\sigma_{bsp}(\lambda)}{\sigma_{sp}(\lambda)} \quad (8)$$

227 g and b are particularly useful for distinguishing aerosol types and assessing their radiative impacts, as backscattering plays a
 228 critical role in determining the cooling efficiency of atmospheric particles.

229 **2.4.3. Back trajectory analysis**

230 The dry optical properties data were paired with a cluster analysis of back trajectories calculated using the
 231 HYSPLIT_4 model from the NOAA Air Resources Laboratory to understand the sources of distinct aerosol types better. The
 232 global data assimilation system (GDAS) at $1^{\circ} \times 1^{\circ}$ resolution (Draxler and Hess, 1998; Stein et al., 2015) was used as
 233 meteorology input, and 72-hour air mass back trajectories arriving at 200 m a.g.l. were calculated every 6 hours. The number
 234 of clusters was estimated based on total spatial variance.

235 **2.4.4. New particle formation events**

236 New Particle Formation (NPF) days were estimated using MPSS Level 1 data ([https://ebas-](https://ebas-submit.nilu.no/templates/Differential-Scanning-Mobility-Particle-Sizer/lev1)
 237 [submit.nilu.no/templates/Differential-Scanning-Mobility-Particle-Sizer/lev1](https://ebas-submit.nilu.no/templates/Differential-Scanning-Mobility-Particle-Sizer/lev1), last accessed: April 2025). Daily heat maps of
 238 concentrations, mode positions, and concentration of particles < 20 nm and between 20 and 100 nm were plotted for every
 239 day, following the Dal Maso et al. (2005) method altered by Németh et al. (2018) for urban stations, each day of the observed
 240 period was classified as either NPF event, non-event, undefined day or missing day.

241 The missing day class (16 out of 304) was assigned when more than 6 hours of the daily measurements were missing,
 242 disabling the classification. Non-event days (67 out of 304) were those where a mode below 25 nm occurred only for a shorter
 243 time than one hour or was absent. Undefined days were identified on 123 days, as the local traffic emissions were often
 244 indistinguishable from potential NPF. NPF days (105 out of 304) were defined as days with a new mode below 25 nm occurring
 245 during the day and with an observable particle size growth for more than 1 hour.

246 **2.4.5. The Principal Component Analysis**

247 To investigate the relationship and underlying patterns between $f(RH)$, $f(RH)_{bsp}$, aerosol particle number
 248 concentration in different modes, meteorological variables, and NPF events, a Principal Component Analysis (PCA) was
 249 performed. The PCA was carried out in R (version 2023.12.0) using the PCA function from the FactoMineR package to reduce
 250 the data's dimensionality and identify dominant modes of variability in the dataset.



Prior to PCA, all variables were standardized (zero mean, unit variance). To handle the remaining missing data without biasing the results, we used a PCA-based imputation method (missMDA package). The optimal number of dimensions for imputation was first estimated using the estim_ncpPCA function; missing values were then imputed using the imputePCA function, which reconstructs incomplete observations based on the relationships captured by the principal components. The first few principal components (Dims) explaining the largest proportion of variance were retained for interpretation based on scree plot analysis and cumulative variance thresholds (Smith, 2002).

3. Results and discussion

3.1. Light scattering properties

The overall median value of dry σ_{sp} at 550 nm (text refers to the overall measurement at $\lambda = 550$ nm unless stated otherwise) was 28.45 Mm^{-1} at the studied site, corresponding to the range of values observed at urban and suburban sites: 14.83 Mm^{-1} at SIRTa (FR), 47.39 Mm^{-1} in Athens (GR), 39.83 Mm^{-1} in Lecce (IT), 18.04 Mm^{-1} and 43.14 Mm^{-1} in Madrid and Granada (ES) (Donateo et al., 2020; Pandolfi et al., 2018).

The dry $\text{SAE}_{450-700}$ value of 1.65, together with a positive median dry ΔSAE (Table 1), indicated a predominantly fine-mode aerosol population, with spectral curvature suggesting the presence of a secondary mode associated with larger particles, likely from aging or mixing processes, similarly to Athens and Granada ($\text{SAE}_{450-700}$ of 1.6 and 1.69), while in Lecce, the fine particle mode dominated ($\text{SAE}_{450-700}$ of 1.84) (Donateo et al., 2020; Pandolfi et al., 2018). The dry b (0.161) and g (0.521) were also typical for urban/suburban environments, suggesting a slightly stronger cooling potential of the aerosol population compared to other sites.

Table 1: The statistics of light scattering properties in the PM_{10} fraction at different wavelengths. P25, P75, and P50 denote the 25th and 75th percentiles and median, respectively. All variables except $f(\text{RH})$ and $f(\text{RH})_{\text{bsp}}$ were measured and calculated at $\text{RH} < 40\%$, and all variables except σ_{sp} and σ_{bsp} are dimensionless.

	λ	Whole period				Fall	Winter	Spring	Summer
		P25	P50	P75	mean \pm SD		P50		
$f(\text{RH})$	450 nm	1.19	1.30	1.42	1.33 ± 0.34	1.20	1.27	1.34	1.33
	550 nm	1.20	1.32	1.44	1.35 ± 0.37	1.22	1.29	1.36	1.34
	700 nm	1.31	1.57	1.93	1.66 ± 0.54	1.46	1.54	1.61	1.63
$f(\text{RH})_{\text{bsp}}$	450 nm	1.07	1.22	1.41	1.25 ± 0.32	1.20	1.20	1.25	1.20
	550 nm	1.04	1.12	1.20	1.14 ± 0.25	1.08	1.10	1.16	1.12
	700 nm	1.11	1.22	1.34	1.25 ± 0.32	1.15	1.20	1.27	1.22
$\sigma_{sp} (\text{Mm}^{-1})$	450 nm	21.81	40.31	80.29	60.99 ± 58.55	99.66	57.14	38.99	33.10
	550 nm	15.54	28.45	56.29	44.19 ± 43.50	73.22	40.84	27.99	22.96
	700 nm	10.89	19.27	36.76	29.93 ± 29.47	48.69	27.27	19.20	15.33
$\sigma_{\text{bsp}} (\text{Mm}^{-1})$	450 nm	3.37	6.05	10.33	8.14 ± 7.27	12.05	7.48	5.74	5.15
	550 nm	2.67	4.72	8.13	6.42 ± 5.70	9.54	5.86	4.56	3.97
	700 nm	2.29	4.08	7.13	5.62 ± 5.04	8.61	5.23	3.95	3.34
$\text{SAE}_{450-700}$		1.45	1.65	1.85	1.61 ± 0.34	1.56	1.57	1.70	1.81
$\text{AAE}_{470-660}$		1.30	1.47	1.62	1.47 ± 0.36	1.58	1.56	1.47	1.26
ΔSAE		-0.091	0.008	0.194	0.063 ± 0.183	-0.122	-0.024	0.056	0.100
SSA b g	550 nm	0.636	0.709	0.766	0.700 ± 0.095	0.650	0.672	0.709	0.755
		0.141	0.161	0.174	0.158 ± 0.027	0.134	0.151	0.163	0.171
		0.492	0.521	0.562	0.528 ± 0.106	0.578	0.542	0.516	0.498

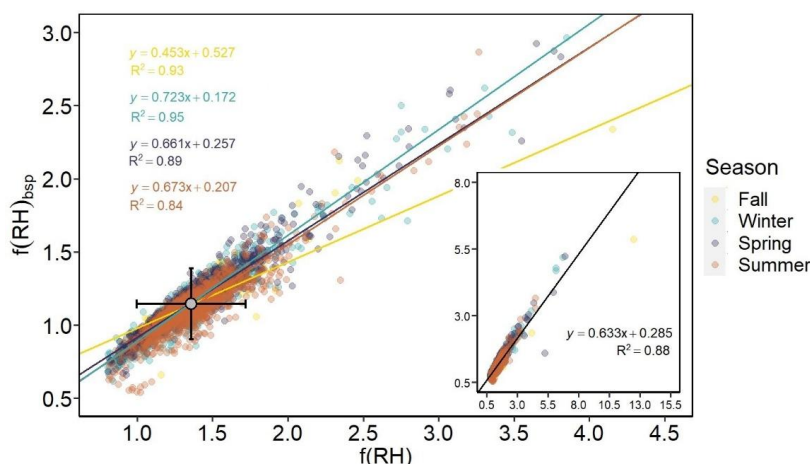
However, a relatively low median value of SSA_{550} (0.709) implies a substantial influence of absorbing aerosol species in the aerosol population. The median $\text{AAE}_{470-660}$ value of 1.47 suggests a relatively balanced contribution of black carbon (BC) and brown carbon (BrC) to aerosol absorption, with a stronger influence of BC in summer ($\text{AAE}_{470-660}$ of 1.26), likely due to



275 traffic emissions. In contrast, elevated AAE values in fall (1.58) and winter (1.56) suggest an increased contribution of BrC
 276 from biomass burning, possibly related to residential heating.

277 3.2. $f(RH)$ and $f(RH)_{bsp}$

278 The overall low enhancement factors $f(RH)$ and $f(RH)_{bsp}$ of 1.32 and 1.12 suggest the influence of low-hygroscopic
 279 carbonaceous aerosol species from local combustion, traffic sources, and their aged derivatives. This result is consistent with
 280 the lower range of $f(RH)$ values observed at urban and suburban sites, for example, average values ranging between 1.32 and
 281 1.74 in a suburban area of Beijing in autumn (Ren et al., 2021), 1.30 near Manacapuru city in Brazil, a site influenced by
 282 industrial activities with soot, high-sulfur oil emissions and biomass burning (Burgos et al., 2019), or 1.5 ± 0.2 in winter in
 283 Granada (Titos et al., 2014).



284 **Figure 4: The weighted bivariate fit of $f(RH)_{bsp}$ vs the $f(RH)$ at $\lambda = 550$ nm in individual seasons. The grey point represents the overall**
 285 **$f(RH)$ and $f(RH)_{bsp}$ mean value with error bars. The inset demonstrates the weighted bivariate fit for the whole dataset.**

286 The $f(RH)_{bsp}$ mimicked the behavior of the $f(RH)$ during the whole year, with the highest correlation in winter (Figure
 287 4). Compared to Titos et al. (2021), our median $f(RH)$ and $f(RH)_{bsp}$ values (gray point in Figure 4) fall into the low enhancement
 288 category of urban sites. Despite the strong linear relationship, $f(RH)_{bsp}$ does not precisely mirror $f(RH)$ and varies with seasons.
 289 As aerosol ERF depends on the hemispheric backscattering ratio b , models relying solely on assumed $f(RH)$ can lead to
 290 inaccurate outcomes (Haywood and Shine, 1995; Hegg et al., 1996; Titos et al., 2021). Such regressions can be beneficial
 291 given the scarcity of $f(RH)_{bsp}$ measurements for modeling enhancement for specific site types. Titos et al. (2021) performed
 292 this fit across several environments (Arctic, marine, rural, and urban) and found the fit equation of $y = 0.55x + 0.32$, $R^2=0.69$
 293 for the Melpitz urban site. Parameters retrieved from our weighted bivariate fit of $f(RH)_{bsp}$ vs the $f(RH)$ can be found in Table
 294 S.3.

295 The $f(RH)$ depends on RH, the particle size, chemical composition, and light wavelength. Its spectral dependence is
 296 crucial for radiative forcing estimates (Fierz-Schmidhauser et al., 2010; Kiehl and Briegleb, 1993; Titos et al., 2021). At the
 297 studied site, the $f(RH)$ increases with wavelength in most cases and seasons except summer (frequency distributions centered
 298 around 0, Fig. S.3), aligning well with results from urban sites (Titos et al., 2021) but showing lower values compared to
 299 marine or Arctic environments. Occasionally, an opposite behavior with a decrease $f(RH)$ with increasing wavelength was
 300 observed, linked to dust episodes and particle size shift (Carrico et al., 2003; Fierz-Schmidhauser et al., 2010).

301 Based on Mie's theory, Hegg et al. (1996) proposed that $f(RH)_{bsp}$ should be approximately 25 % lower than $f(RH)$ for
 302 typical atmospheric aerosols. Our observations support this, showing consistently smaller $f(RH)_{bsp}$ than $f(RH)$ across all



wavelengths. On average, $f(RH)_{bsp}$ was lower by 6 %, 15 %, and 22 % at 450, 550, and 700 nm, respectively, with the largest differences observed in summer reaching 10 %, 16 %, and 25 %. The relative difference between $f(RH)$ and $f(RH)_{bsp}$ increases with wavelength, suggesting a spectral sensitivity of backscattering to humidification, likely due to particle size and composition effects on the angular distribution of scattered light. These findings highlight the need for wavelength- and season-specific correction factors when using $f(RH)$ to estimate aerosol backscattering or when interpreting satellite data sensitive to the backscattered light.

The probability density functions of $f(RH)$ and $f(RH)_{bsp}$ for different wavelengths can be found in Fig. S.4.

3.3. Seasonal variability

The lowest $f(RH)$ and $f(RH)_{bsp}$ values were observed in the fall, with a monthly minimum in November (1.22 and 1.07, Figure 5). Both peaked in spring, with a monthly maximum in May (1.40 and 1.19). The increase from autumn to spring was interrupted in March when both $f(RH)$ and $f(RH)_{bsp}$ dropped to 1.22 and 1.08, probably due to March being a transitional period between winter and spring in the Northern Hemisphere. Although this anomaly has not been fully understood yet, CAMS reanalysis by Flemming et al. (2017) also identified irregular springtime atmospheric patterns over the Northern Hemisphere, while Suchánková et al. (2025) observed a steep increase in dry σ_{sp} and σ_{bsp} , and ultrafine and fine particle number concentration at an urban site in France. After peaking in May, both $f(RH)$ and $f(RH)_{bsp}$ gradually decreased towards August (1.34 and 1.12). The seasonal variation is consistent with results reported at the urban site in Granada (Titos et al., 2014).

Lower values of $f(RH)$ and $f(RH)_{bsp}$ in fall and winter suggest the prevalence of low-hygroscopic aerosol species, such as carbonaceous particles from combustion and traffic sources. In summer and spring, the enhancement is influenced by hygroscopic SOA, as supported by the statistically significant Spearman correlations between $f(RH)/f(RH)_{bsp}$ and SSA_{550} ($R = 0.31/0.23$). Although SSA_{550} peaks in summer, likely due to highly hygroscopic secondary organic and inorganic aerosols (sulfates and nitrates), the strongest correlation between $f(RH)/f(RH)_{bsp}$ and SSA_{550} is in spring ($R = 0.34/0.27$). Sulfates and nitrates amplify aerosol hygroscopicity more effectively than organic matter, especially compared to the less hygroscopic organic species prominent in summer. This seasonal contrast highlights the key role of inorganic species like sulfate and nitrate in controlling aerosol optical properties through their impact on hygroscopic growth. During spring, the aerosol composition is relatively homogeneous, dominated by aged, regionally transported aerosols with intermediate hygroscopicity, resulting in stronger and more predictable correlations between enhancement factors and SSA_{550} . While both spring and summer can include biogenic organics and aged urban particles, the chemical composition in summer is more variable, leading to less consistent hygroscopic behavior and the weakest seasonal correlations with SSA_{550} ($R = 0.16/0.17$).

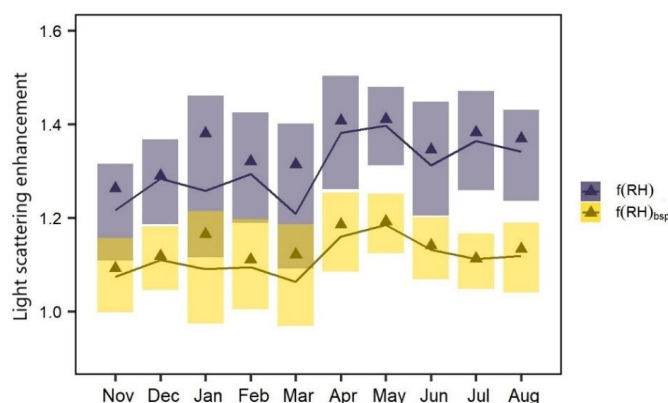


Figure 5: The monthly variation of the $f(RH)$ and the $f(RH)_{bsp}$ measured at 550 nm. The lines with shaded areas depict the median with the interquartile range, and the triangles represent mean values.



The temporal variation of $f(RH)$ did not show any consistent connection to $SAE_{450-700}$ (Fig. S.5a). The $SAE_{450-700}$ values rise from colder months to warmer months, suggesting the presence of smaller particles from the NPF or the traffic. Compared to winter, the enhanced mixing and higher dilution due to the higher planetary boundary layer height (PBLH) in spring and summer also prevent particle growth due to condensation. This statement was supported by the analysis of particle number size distribution (PNSD), with D_p below 200 nm primarily present in the photooxidatively active time of the year. At the same time, larger particles occurred mainly in colder seasons (Fig. S.6). However, the nephelometer does not precisely measure the ultrafine particle sizes due to its geometry and principle of operation, possibly distorting the direct relationship between the light scattering enhancement and PNSD.

While we found a larger influence of the chemical composition on light scattering enhancement than the particle size, the seasonal variations in the ratio b were linked to changes in aerosol size distributions and sources. Smaller particles (higher $SAE_{450-700}$ values in warmer months) typically exhibit a higher backscattering fraction under dry conditions; however, their hygroscopic growth may lead to a relative decrease in backscattering enhancement compared to total scattering due to changes in the scattering phase function (Fig. S.5b).

3.4. Light scattering enhancement vs other aerosol-intensive optical properties

Understanding the relationship between light scattering enhancement and other aerosol optical properties can help improve the characterization of aerosol types and their radiative impacts.

$SAE_{450-700} > 1$ mirrored the frequency distribution of both $f(RH)$ and $f(RH)_{bsp}$ (Figure 6). A slight shift towards more hygroscopic behavior was observed for $SAE_{450-700} < 1$ in $f(RH)_{bsp}$. In contrast, $SSA_{550} < 0.6$ exhibits a shift to the left for both $f(RH)$ and $f(RH)_{bsp}$, indicating an overall significant decreasing effect of absorbing aerosol species on aerosol light scattering enhancement, consistent with the finding of Titos et al. (2014).

In winter and spring, particles with $SAE_{450-700} < 1$ showed slightly more hygroscopic behavior both for $f(RH)$ and $f(RH)_{bsp}$, possibly due to the internal mixtures of sulfates and nitrates or the presence of mineral dust. Particles characterized with $SSA_{550} < 0.6$ consistently showed lower $f(RH)$ and $f(RH)_{bsp}$ values. In spring and summer, the frequency distribution of $SSA_{550} > 0.6$ mimicked the whole dataset distribution, implying a higher share of light-scattering aerosols (Fig. S.7).

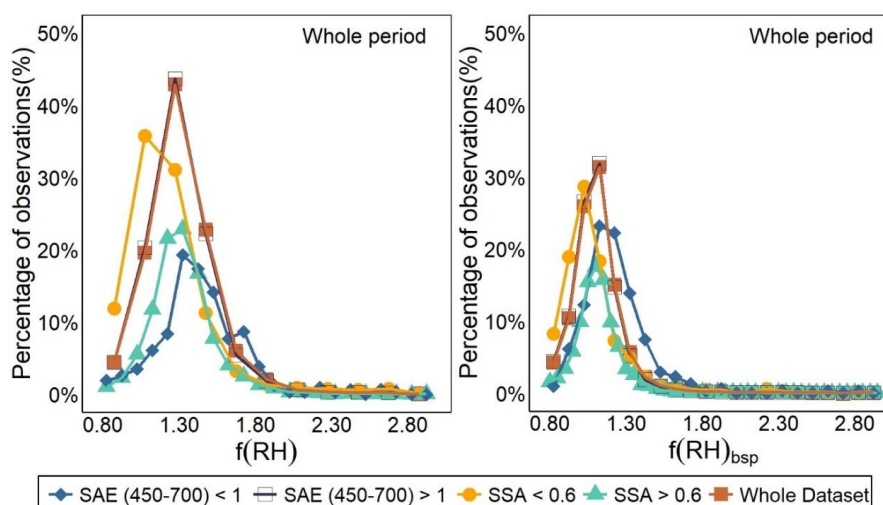
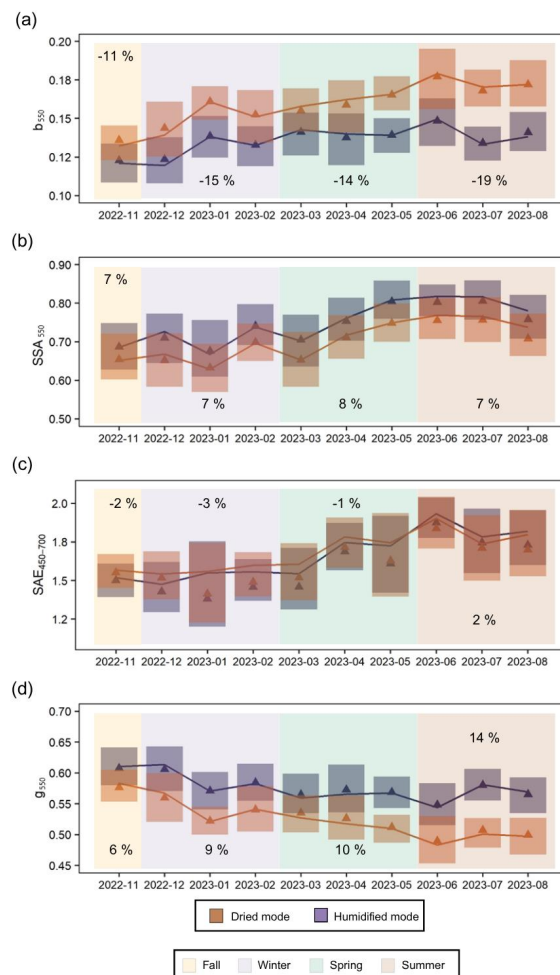


Figure 6: Frequency distribution of $f(RH)$ (left) and $f(RH)_{bsp}$ (right) calculated at 550 nm during the whole measurement campaign. The distributions are color and symbol-coded based on $SAE_{450-700}$ and SSA_{550} values.



361 Dry SSA_{550} was lower for less hygroscopic particles ($f(RH) < 1.5$) than for more hygroscopic ones ($f(RH) > 1.5$),
 362 0.708 vs 0.742 (Fig. S.8a), confirming the adverse effect of absorbing components on hygroscopicity. Across all seasons, the
 363 SSA increased with RH (Figure 7b), while b_{550} showed the opposite behavior (Figure 7a), as expected, given their inverse
 364 relationship. This relationship was more pronounced under humidified conditions than dried ones (Fig. S.8b) (Burgos et al.,
 365 2020; Titos et al., 2021). As particles take up water and grow, the total scattering increases with a predominance of the forward
 366 light scattering over backscattering.



367
 368 **Figure 7: The monthly variation of b_{550} (a), SSA_{550} (b), $SAE_{450-700}$ (c), and g_{550} (d) at dried and humidified conditions in individual**
 369 **seasons (colored background). A percentage value in each season shows a relative change between humidified and dried median**
 370 **values for the respective season. The lines with shaded areas depict the median and the interquartile range, and the triangles**
 371 **represent respective mean values.**

372 The asymmetry factor g_{550} also increased with RH , confirming stronger forward than backward scattering with enhanced
 373 RH (Figure 7d). The $SAE_{450-700}$ decreased with increasing RH , indicating particle size growth in all seasons except summer
 374 (Figure 7c). During summer, an atypical behavior of the $SAE_{450-700}$ was observed, with dry particles appearing optically larger
 375 (lower SAE) than the humidified ones. This is likely linked to the dominance of BC-rich aerosols, which are weakly
 376 hygroscopic and maintain large agglomerated structures in the dry state. Such structures may compact upon humidification,



reducing optical growth and increasing SAE. This behavior contrasts with highly hygroscopic sulfate- or nitrate-rich aerosol regimes, where humidification leads to particle growth and lower SAE values.

Comparing our site with those reported by Titos et al. (2021), we found the lowest $f(RH)$, similar to urban (e.g., Manacapuru, Brazil, and Nainital, India), desert (Niamey, Niger), and some rural (e.g., Hyytiälä, Finland) environments. Interestingly, the SSA_{550} at our site was the lowest, indicating a strong presence of absorbing aerosols such as black carbon or other combustion-related species (Fig. S.5c). This confirms the role of local or regional combustion sources in shaping aerosol optical properties.

3.5. The estimation of chemical composition from optical properties

Due to the lack of direct measurement of chemical composition at the site, we used the approach introduced by Cappa et al. (2016), using $AAE_{520-660}$, $SAE_{450-550}$, and SSA_{550} to estimate the aerosol chemical composition. Aerosol at the station was found mainly in the fine fraction, dominated by BC in a mixture with BrC (Figure 8), in agreement with the low $f(RH)$ and $f(RH)_{bsp}$ at the site. The site was also influenced by BC and BrC in a mixture with dust, probably coming from the road dust, although unexamined Saharan dust episodes may have contributed. These mixtures included large, poorly absorbing coated particles and locally emitted sulfates and nitrates in the fine size mode, which highly scatter but weakly absorb the incoming light.

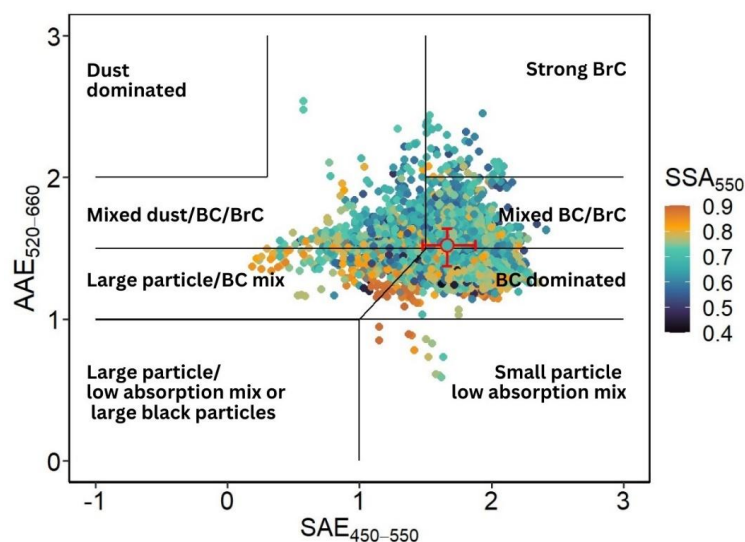


Figure 8: $AAE_{520-660}$ vs. $SAE_{450-550}$ hourly means from the whole campaign, color-coded with SSA_{550} overlaid with the aerosol characterization matrix adopted from Cappa et al. (2016) and Cazorla et al. (2013). The red circle with red error bars estimated the median $AAE_{520-660}$ – $SAE_{450-550}$ point with interquartile ranges.

SSA_{550} values were equally distributed among the plot regions, except for the highest values in the aerosol mixture of sea salt, dust, and low-absorbing coated particles with BC and BrC. Such aerosol was typically connected with air masses coming from Poland and Eastern Europe (Figure 9). High concentrations of the mixture with BrC were observed in fall, winter, and spring, predominantly due to biomass burning. Consequently, the median $AAE_{520-660}$ vs. $SAE_{450-550}$ point fell into the 'Mixed/BC/BrC' plot region. In contrast, the BC aerosol mixture started to dominate in spring and summer (Fig. S.9).

Although multiple wintertime clusters originated from the marine regions, only Cluster 6 (Figure 9a) shifted towards dust/large low-absorbing particle aerosol mixture, indicating the influence of fossil fuel/biomass burning sources during this



season. In spring, the air masses of Clusters 2 and 4 originated from the Norwegian Sea and Atlantic Ocean (Figure 9b) and featured hygroscopic sea salt mixtures. In summer, the BC-dominated aerosol prevailed (Figure 9c); however, marine clusters (Clusters 1, 4, and 5) shifted towards larger aerosol sizes, suggesting aerosol-aged mixtures influencing the ability to scatter and absorb radiation.

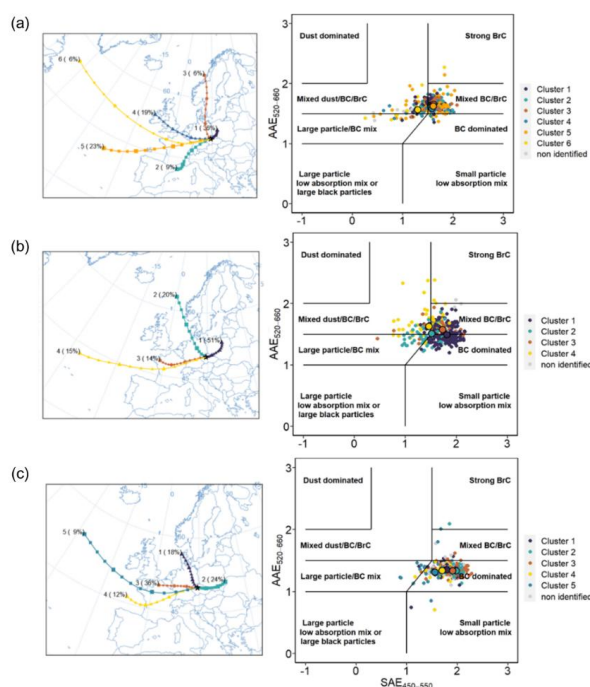
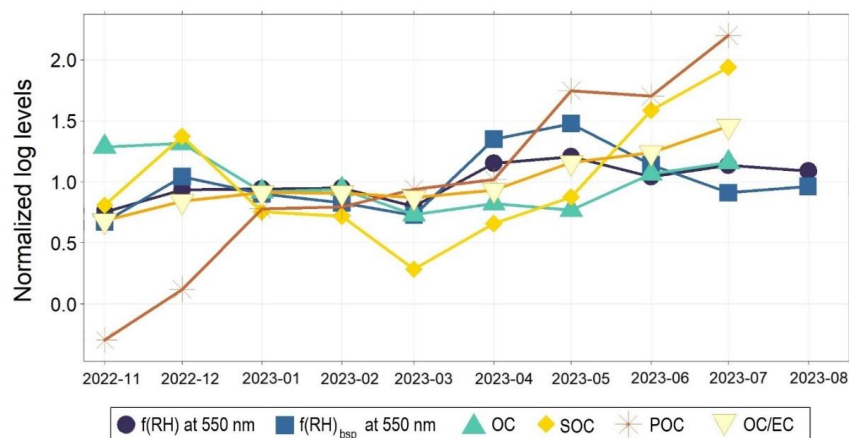


Figure 9: The 72-h air mass back trajectories paired with AAE₅₂₀₋₆₆₀ vs SAE₄₅₀₋₅₅₀ for winter (a), spring (b), and summer (c). The plots are color-coded by trajectory cluster number, with cluster medians indicated by black circles and the percentage contribution of each cluster provided. The fall was not taken into consideration due to the limited data.

To investigate seasonal variations in BC aerosol concentration, semi-online OC/EC measurements were used to calculate the concentrations of the secondary (SOC) and primary (POC) organic carbon based on the method used in Mbengue et al. (2021). The concentrations of OC, POC, SOC, and the ratio of organic and elemental carbon (OC/EC) remained stable during winter and increased in spring, mirroring the behavior of $f(RH)$ until May (Figure 10). However, carbonaceous components rose from late spring into summer while mainly $f(RH)_{bsp}$ decreased, suggesting a seasonal decoupling of SOC and aerosol hygroscopicity. This may be due to the higher fraction of POC (Liu and Wang, 2010), the formation of less hygroscopic SOA from biogenic precursors (Huang et al., 2019), and the evaporation of semi-volatile organics at higher temperatures, reducing their contribution to water uptake and $f(RH)$ (Thomsen et al., 2024).



419

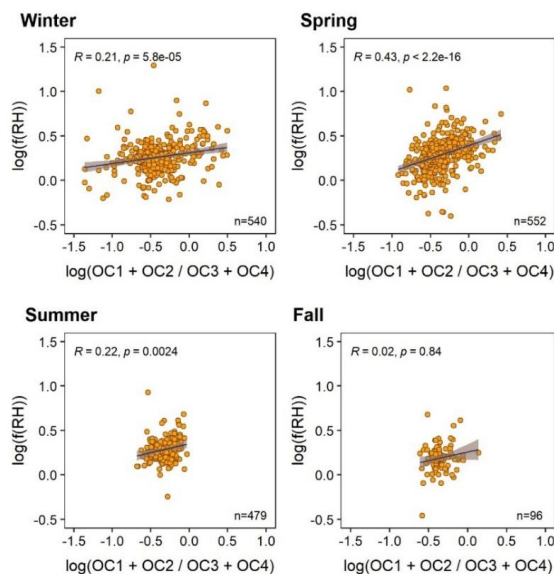
420 **Figure 10: Mean-normalized temporal variation of logarithm of 4-h median values of $f(RH)$ and $f(RH)_{bsp}$, OC, SOC, POC, and**
 421 **OC/EC.**

422 Elemental carbon (EC) showed negative Spearman correlations with $f(RH)$ and $f(RH)_{bsp}$ ($R = -0.33$ and -0.17), as
 423 expected. OC showed a moderate negative correlation with $f(RH)$, yet the OC/EC ratio correlated positively with $f(RH)$ and
 424 $f(RH)_{bsp}$, especially during spring ($R = 0.31$). This indicates that the relative abundance of organic carbon, rather than its
 425 absolute concentration, enhances hygroscopicity (Table S.4). The SOC/OC ratio seasonal behavior followed the OC/EC
 426 seasonality, emphasizing the role of SOA in aerosol hygroscopic growth.

427 The four OC subfractions distinguished by the thermo-optical method further clarified this behavior. Surprisingly,
 428 the sum of more volatile OC1 and OC2 positively correlates with $f(RH)$. In contrast, the sum of less volatile OC3 and OC4
 429 showed negative correlations, implying higher hygroscopicity of fresher, more volatile OC subfractions (Figure 11). This
 430 aligns with field studies of “smoke” particles by Chan et al. (2005), showing that levoglucosan from biomass burning or urban
 431 pollution can “age” into simpler dicarboxylic acids, such as succinic acid, which is less hygroscopic than the original substance,
 432 causing aged biomass burning aerosols to be less hygroscopic than the fresh ones. However, the hygroscopicity of the
 433 mentioned organic compounds highly depends on their mixing state and the additional components in the mixture (Maskey et
 434 al., 2014).

435 A key factor influencing this trend may be Humic-Like Substances (HULIS), typically associated with OC3 and OC4.
 436 HULIS are low in volatility and hygroscopicity (Kristensen et al., 2012) and are primarily emitted from biomass burning,
 437 residential heating, and traffic. Their presence may suppress water uptake and light scattering (Dinar et al., 2008). Urban
 438 HULIS tend to absorb light more and decrease SSA than rural sources (Tang et al., 2020). HULIS often exist in the glassy or
 439 semi-solid state, preventing diffusion of water molecules in their structure and decreasing their hygroscopicity (Koop et al.,
 440 2011), and further, aging can enhance viscosity via oligomerization, reducing hygroscopicity even more (Song et al., 2016).

441 The highest correlation between $f(RH)$, $f(RH)_{bsp}$, and $(OC1 + OC2)/(OC3 + OC4)$ ratio was found in spring ($R=0.43$
 442 and 0.28) despite stronger photochemical activity during summer (Figure 11). This counterintuitive result suggests that spring
 443 conditions preserve more water-uptake-efficient OC1 and OC2 in the particulate phase, while intense summer photochemistry
 444 and higher temperatures drive oxidation and oligomerization of organic compounds, transforming initially hygroscopic semi-
 445 volatile organics ($OC1+OC2$) into more aged, less hygroscopic fractions ($OC3+OC4$), and promote volatile organics
 446 evaporation, reducing the relative contribution of fresh OC to the particulate phase.



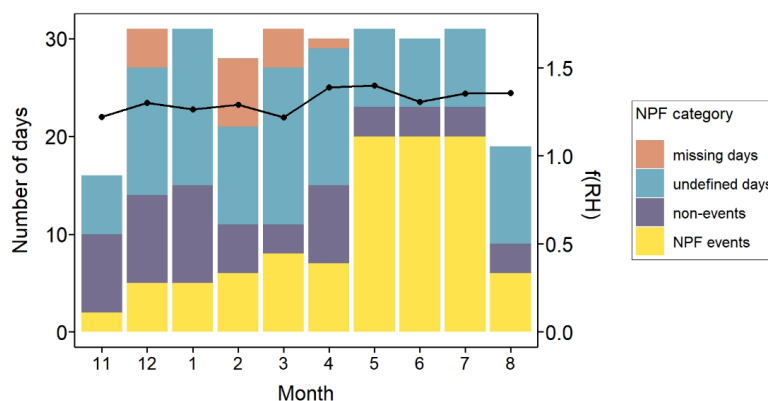
447

448 **Figure 11: Seasonal Spearman correlations between the $f(RH)$ and the log-transformed ratio of more volatile OC fractions**
 449 **(OC1+OC2) and less volatile OC fractions (OC3+OC4). The values in the bottom right corner indicate the number of observations,**
 450 **and the values in the upper left corner indicate Spearman correlation coefficient R and the respective p values.**

451 3.6. Light scattering enhancement and NPF

452 Previous chapters suggested a link between light scattering enhancement and secondary particles originating from NPF,
 453 supporting the results of Liu et al. (2022) and Mitra et al. (2022) on a considerable role of SOA in the light scattering
 454 enhancement and the respective aerosol radiative impacts.

455 The highest number of NPF events were found in May, June, and July, correlating with the highest $f(RH)$ in May (Figure 12).
 456 However, despite continued NPF activity, $f(RH)$ decreased in June and July, implying a shift in aerosol chemical composition.
 457 Chemical composition estimation and absorption measurements point to traffic-related BC during summer months, which
 458 diminishes the effect of secondary particle growth on light scattering enhancement.



459

460 **Figure 12: Monthly NPF events classification and $f(RH)$ median values (black line).**



The principal component analysis (PCA) was performed using meteorological variables and particle number concentrations to investigate the role of NPF in the observed seasonal variability of light scattering enhancement. In May, particle number concentrations in the 8–100 nm size range ($D_{p_8_100}$) strongly correlated with high global radiation (GLRD), temperature (T), and ozone (O_3), conditions favorable for photochemical activity (Fig. S.10). Also PNSD analyzed during daytime NPF events from March to August showed high 20 nm peak in May (ca. 8,000 # cm⁻³, Figure 13), and the PNSD's 75th percentile shifted toward smaller diameters compared to other months, indicating more intense or more frequently initiated NPF events, driven by favorable precursor conditions. Interestingly, August exhibited an even higher concentration of 20 nm peak (ca. 10,000 # cm⁻³) than May, but with only 10 NPF days and no clear correlation of $D_{p_8_100}$ with environmental variables.

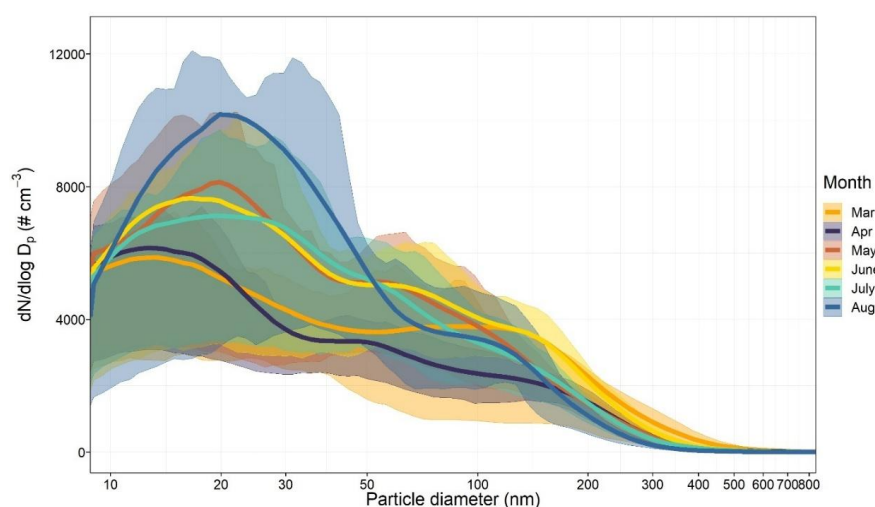


Figure 13: The particle size number distributions during NPF days from 7:30 AM to 7:30 PM UTC.

From diurnal analysis of PNSD in May and August, additional differences in the aerosol populations were found (Fig. S.11). In May, morning PNSD displayed a bimodal distribution peaking at 15 nm and 60 nm, reaching ca. 5,000 and 6,000 # cm⁻³ in medians, originating from newly formed ultrafine particles and aged background particles. By midday, the distribution was dominated by freshly nucleated particles in the 15–20 nm range, with concentrations peaking at around 12,000 # cm⁻³, shifting to ca 7,000 # cm⁻³ 30 nm peak in the afternoon due to the growth and coagulation of the particles.

In August, morning PNSDs were also bimodal, with a dominating 15 nm peak (10,000 # cm⁻³) and a second peak at 55 nm (6,000 # cm⁻³). The peak diameter moved to 25 nm (14,000 # cm⁻³) in midday and 40 nm (11,000 # cm⁻³) in late afternoon. Although August exhibited higher concentrations and stronger growth during selected NPF events, the $f(RH)$ was lower in August (~1.34) than in May (~1.40), indicating limited growth of ultrafine particles formed in August to optically active sizes. On the other hand, the higher May $f(RH)$ values reflect a combination of efficient particle growth, the higher hygroscopicity of condensable vapors, and possibly lower background aerosol surface area, promoting nucleation and early growth stages. These results highlight that NPF frequency, and its intensity alone do not determine optical relevance - hygroscopic growth potential, size evolution of particles, and chemical composition of the condensing vapors are also crucial for determining aerosol radiative impacts.



486 4. Summary and conclusions

487 This work presented a novel, cost-effective approach to investigate aerosol hygroscopicity using a single-nephelometer
 488 set-up with an automatically controlled switching valve alternating between humidified and dried sample branches. This design
 489 reduces uncertainties associated with dual-instrument configurations. After testing and calibrations, the system was installed
 490 at the suburban site, Suchdol in Prague, Czech Republic, from November 2022 to August 2023 to fill the knowledge gap related
 491 to the optical hygroscopic behavior of aerosol at European urban/suburban sites, particularly regarding light scattering under
 492 increased relative humidity (RH).

493 The light total scattering enhancement factor $f(RH)$ and the light backscattering enhancement factor $f(RH)_{bsp}$ were derived
 494 from the humidified and dried measurement of the light total scattering (σ_{sp}) and backscattering (σ_{bsp}) coefficients at 450, 550,
 495 and 700 nm. The enhancements were analyzed in relation to climate-relevant aerosol optical properties —
 496 Scattering/Absorption Ångström Exponent SAE/AAE, hemispheric backscattering ratio b , asymmetry factor g , and Single
 497 Scattering Albedo SSA — estimated chemical composition, particle number size distributions (PNSD), meteorological
 498 parameters, back trajectory analysis, and new particle formation (NPF) events.

499 The measured $f(RH)$ and $f(RH)_{bsp}$ at 550 nm were among the lowest (1.32 and 1.12 at 550 nm), together with one of
 500 the lowest SSA_{550} reported in similar studies. This indicates a dominance of low-hygroscopic aerosol species originating from
 501 local combustion and traffic emissions. The seasonal and wavelength-specific differences in the relationship between $f(RH)_{bsp}$
 502 and $f(RH)$ underscore the importance of specific corrections in radiative models. Peaks of $f(RH)$ and $f(RH)_{bsp}$ were detected in
 503 spring, possibly caused by the higher presence of more hygroscopic aerosol and enhanced photochemical activity. An increase
 504 of $f(RH)$ and $f(RH)_{bsp}$ resulted in decreased b_{550} and increased g_{550} and SSA_{550} , implying enhanced total scattering and stronger
 505 forward scattering for larger particles caused by hygroscopic growth. However, $SAE_{450-700}$ increased with RH in summer,
 506 indicating shrinking of particles, possibly due to the very low-hygroscopic black carbon (BC) emissions prone to compacting
 507 upon humidification.

508 Chemical composition ruled the light scattering enhancement at the site more than PNSD. BC-dominated aerosol
 509 prevailed in summer, while other seasons featured aerosol mixtures with BC and BrC, occasionally dust and marine aerosol.
 510 Both $f(RH)$ and $f(RH)_{bsp}$ correlated positively with OC/EC and SOC/OC ratios. The more volatile organic fractions exhibited
 511 a positive correlation with the light scattering enhancement compared to the less volatile ones, mainly in the spring season,
 512 highlighting the critical role of SOC in the overall aerosol hygroscopicity despite their low-hygroscopic potential, mainly at
 513 polluted sites. The principal component analysis (PCA), the PNSD, and the NPF analysis identified May as the month when
 514 NPF most strongly contributed to the overall light scattering enhancement.

515 In summary, the single-nephelometer system proved suitable for ambient aerosol characterization, reducing measurement
 516 uncertainty. However, the limits of this kind of measurement are the reduced time resolution, together with a lack of parallel
 517 measurement of dry and wet aerosol properties for humidogram studies. Our findings contribute to filling a key gap in the
 518 global dataset by providing insight into environments where low $f(RH)$, low SSA, and relatively high SAE co-occur —
 519 conditions that are underrepresented in the literature.

520 Authors contribution

521 LS, JO, PR and VZ designed the methodology of the work and created the study conceptualization. Additionally, LS was
 522 responsible for data curation, formal analysis, investigation, validation, software, visualization, and writing of the original
 523 draft. JO was responsible for software, resources, investigation, and writing — review & editing. NZ contributed to data
 524 curation, formal analysis and writing — review & editing. PR was additionally responsible for software. PV was responsible
 525 for data curation and writing — review & editing. RP was responsible for project administration, funding and administration and
 526 writing — review & editing. IH contributed to supervision. VZ was responsible for project administration, supervision,
 527 resources and writing — review & editing.



528 Data availability

529 Datasets including $f(RH)$ and $f(RH)_{bsp}$, original relative humidity and temperature variation within humidified single-
 530 nephelometer set-up system, concentration of carbonaceous aerosol species, particle size number concentration,
 531 meteorological parameters, dry and humidified aerosol optical properties, NPF categorization, and air mass back-trajectory
 532 cluster identification are available at Suchánková, Lenka (2025), “Humidified single-nephelometer set-up system datasets”,
 533 Mendeley Data, V1, doi: 10.17632/8ds98t2f3x.1.

534 Competing interests

535 The authors declare that have no competing interests.

536 Acknowledgments

537 This work was supported by the Ministry of Education, Youth and Sports of the CR within the Large Research Infrastructure
 538 ACTRIS Czech Republic (LM2023030) and CzeCOS (LM2023048). The authors thank the RECETOX RI (No LM2023069)
 539 for the supportive background. This work was supported by the European Union's Horizon 2020 research and innovation
 540 program under grant agreement No 857560 (CETOCOEN Excellence). This publication reflects only the author's view, and
 541 the European Commission is not responsible for any use that may be made of the information it contains. Authors acknowledge
 542 support from AdAgriF - Advanced methods of greenhouse gases emission reduction and sequestration in agriculture and forest
 543 landscape for climate change mitigation (CZ.02.01.01/00/22_008/0004635).

544 References

- 545 Alduchov, O. A. and Eskridge, R. E.: Magnus-Tetens formula, Asheville, 21 pp.,
 546 <https://doi.org/https://doi.org/10.2172/548871>, 1997.
- 547 Anderson, T. L. and Ogren, J. A.: Determining Aerosol Radiative Properties Using the TSI 3563 Integrating Nephelometer,
 548 *Aerosol Sci. Technol.*, 29, 57–69, <https://doi.org/10.1080/02786829808965551>, 1998.
- 549 Anderson, T. L., Covert, D. S., Marshall, S., Laucks, M. L., Charlson, R. J., Waggoner, A. P., Ogren, J. A., Caldow, R., Holm,
 550 R. L., Quant, F. R., Sem, G. J., Wiendensholer, A., Ahlquist, N. A., and Bates, T. S.: Performance Characteristics of a High-
 551 Sensitivity, Three-Wavelength, Total Scatter/Backscatter Nephelometer, *Cover J. Atmos. Ocean. Technol. J. Atmos. Ocean.*
 552 *Technol.*, 13, 967–986, [https://doi.org/https://doi.org/10.1175/1520-0426\(1996\)013<0967:PCOAHS>2.0.CO;2](https://doi.org/https://doi.org/10.1175/1520-0426(1996)013<0967:PCOAHS>2.0.CO;2), 1996.
- 553 Andrews, E., Sheridan, P. J., Fiebig, M., McComiskey, A., Ogren, J. A., Arnott, P., Covert, D., Elleman, R., Gasparini, R.,
 554 Collins, D., Jonsson, H., Schmid, B., and Wang, J.: Comparison of methods for deriving aerosol asymmetry parameter, *J.*
 555 *Geophys. Res. Atmos.*, 111, D05S04, <https://doi.org/10.1029/2004JD005734>, 2006.
- 556 Aswini, A. R., Hegde, P., Nair, P. R., and Aryasree, S.: Seasonal changes in carbonaceous aerosols over a tropical coastal
 557 location in response to meteorological processes, *Sci. Total Environ.*, 656, 1261–1279,
 558 <https://doi.org/10.1016/J.SCITOTENV.2018.11.366>, 2019.
- 559 Bauer, J. J., Yu, X.-Y., Cary, R., Laulainen, N., and Berkowitz, C.: Characterization of the sunset semi-continuous carbon
 560 aerosol analyzer., *J. Air Waste Manag. Assoc.*, 59, 826–833, <https://doi.org/10.3155/1047-3289.59.7.826>, 2009.
- 561 Boucher, O.: Atmospheric Aerosols, in: *Atmospheric Aerosols*, Springer Netherlands, Dordrecht, 9–24,
 562 https://doi.org/10.1007/978-94-017-9649-1_2, 2015.
- 563 Burgos, M. A., Andrews, E., Titos, G., Alados-Arboledas, L., Baltensperger, U., Day, D., Jefferson, A., Kalivitis, N.,



- 564 Mihalopoulos, N., Sherman, J., Sun, J., Weingartner, E., and Zieger, P.: A global view on the effect of water uptake on aerosol
 565 particle light scattering, *Sci. Data*, 6, 1–19, <https://doi.org/10.1038/s41597-019-0158-7>, 2019.
- 566 Burgos, M. A., Andrews, E., Titos, G., Benedetti, A., Bian, H., Buchard, V., Curci, G., Kipling, Z., Kirkevåg, A., Kokkola,
 567 H., Laakso, A., Letertre-Danczak, J., T. Lund, M., Matsui, H., Myhre, G., Randles, C., Schulz, M., Van Noije, T., Zhang, K.,
 568 Alados-Arboledas, L., Baltensperger, U., Jefferson, A., Sherman, J., Sun, J., Weingartner, E., and Zieger, P.: A global model-
 569 measurement evaluation of particle light scattering coefficients at elevated relative humidity, *Atmos. Chem. Phys.*, 20, 10231–
 570 10258, <https://doi.org/10.5194/ACP-20-10231-2020>, 2020.
- 571 Cappa, C. D., Kolesar, K. R., Zhang, X., Atkinson, D. B., Pekour, M. S., Zaveri, R. A., Zelenyuk, A., and Zhang, Q.:
 572 Understanding the optical properties of ambient sub- and supermicron particulate matter: Results from the CARES 2010 field
 573 study in northern California, *Atmos. Chem. Phys.*, 16, 6511–6535, <https://doi.org/10.5194/acp-16-6511-2016>, 2016.
- 574 Carrico, C. M., Kus, P., Rood, M. J., Quinn, P. K., Bates, T. S., Carrico, C. :, Kus, P., Rood, M. J., Quinn, P. K., and Bates, T.
 575 S.: Mixtures of pollution, dust, sea salt, and volcanic aerosol during ACE-Asia: Radiative properties as a function of relative
 576 humidity, *J. Geophys. Res. Atmos.*, 108, 8650, <https://doi.org/10.1029/2003JD003405>, 2003.
- 577 Carslaw, K. S., Gordon, H., Hamilton, D. S., Johnson, J. S., Regayre, L. A., Yoshioka, M., and Pringle, K. J.: Aerosols in the
 578 Pre-industrial Atmosphere, *Curr. Clim. Chang. Reports* 2017 31, 3, 1–15, <https://doi.org/10.1007/S40641-017-0061-2>, 2017.
- 579 Cavalli, F., Viana, M., Yttri, K. E., Genberg, J., and Putaud, J. P.: Toward a standardized thermal-optical protocol for measuring
 580 atmospheric organic and elemental carbon: The EUSAAR protocol, *Atmos. Meas. Tech.*, 3, 79–89,
 581 <https://doi.org/10.5194/amtd-2-2321-2009>, 2010.
- 582 Cazorla, A., Bahadur, R., Suski, K. J., Cahill, J. F., Chand, D., Schmid, B., Ramanathan, V., and Prather, K. A.: Relating
 583 aerosol absorption due to soot, organic carbon, and dust to emission sources determined from in-situ chemical measurements,
 584 *Atmos. Chem. Phys.*, 13, 9337–9350, <https://doi.org/10.5194/acp-13-9337-2013>, 2013.
- 585 Statistický atlas - ČSÚ:
 586 [https://geodata.csu.gov.cz/as/atlas/?xmax=2194777.485518976&ymax=6694180.788553198&xmin=1255519.2819509797&](https://geodata.csu.gov.cz/as/atlas/?xmax=2194777.485518976&ymax=6694180.788553198&xmin=1255519.2819509797&ymin=6135884.7339584185&wkid=102100)
 587 [ymin=6135884.7339584185&wkid=102100](https://geodata.csu.gov.cz/as/atlas/?xmax=2194777.485518976&ymax=6694180.788553198&xmin=1255519.2819509797&ymin=6135884.7339584185&wkid=102100), last access: 13 December 2024.
- 588 Chan, M. N., Choi, M. Y., Ng, N. L., and Chan, C. K.: Hygroscopicity of water-soluble organic compounds in atmospheric
 589 aerosols: Amino acids and biomass burning derived organic species, *Environ. Sci. Technol.*, 39, 1555–1562,
 590 <https://doi.org/10.1021/ES049584L>, 2005.
- 591 Clarke, A. and Kapustin, V.: Hemispheric aerosol vertical profiles: Anthropogenic impacts on optical depth and cloud nuclei,
 592 *Science*, 329, 1488–1492, https://doi.org/10.1126/SCIENCE.1188838/SUPPL_FILE/CLARKE.SOM.PDF, 2010.
- 593 Covert, D. S., Charlson, R. J., and Ahlquist, N. C.: A Study of the Relationship of Chemical Composition and Humidity to
 594 Light Scattering by Aerosols, *J. Appl. Meteorol.*, 11, 968–976, [https://doi.org/10.1175/1520-0450\(1972\)011<0968:asotro>2.0.co;2](https://doi.org/10.1175/1520-0450(1972)011<0968:asotro>2.0.co;2), 1972.
- 596 Dal Maso, M., Kulmala, M., Riipinen, I., Wagner, R., Hussein, T., Aalto, P. P., and Lehtinen, K. E. J.: Formation and growth
 597 of fresh atmospheric aerosols: eight years of aerosol size distribution data from SMEAR II, Hyytiälä, Finland, *Boreal Environ.*
 598 *Res.*, 10, 323–336, 2005.
- 599 Dinar, E., Abo Riziq, A., Spindler, C., Erlick, C., Kiss, G., and Rudich, Y.: The complex refractive index of atmospheric and
 600 model humic-like substances (HULIS) retrieved by a cavity ring down aerosol spectrometer (CRD-AS), *Faraday Discuss.*,
 601 137, 279–295, <https://doi.org/10.1039/B703111D>, 2008.



- 602 Doherty, S. J.: A comparison and summary of aerosol optical properties as observed in situ from aircraft, ship, and land during
603 ACE-Asia, *J. Geophys. Res.*, 110, D04201, <https://doi.org/10.1029/2004JD004964>, 2005.
- 604 Donato, A., Lo Feudo, T., Marinoni, A., Calidonna, C. R., Contini, D., and Bonasoni, P.: Long-term observations of aerosol
605 optical properties at three GAW regional sites in the Central Mediterranean, *Atmos. Res.*, 241, 104976,
606 <https://doi.org/10.1016/j.atmosres.2020.104976>, 2020.
- 607 Draxler, R. R. and Hess, G. D.: An overview of the HYSPLIT_4 modelling system for trajectories, dispersion and deposition,
608 1998.
- 609 Fierz-Schmidhauser, R., Zieger, P., Gysel, M., Kammermann, L., Decarlo, P. F., Baltensperger, U., and Weingartner, E.:
610 Measured and predicted aerosol light scattering enhancement factors at the high alpine site Jungfraujoch, *Atmos. Chem. Phys.*,
611 10, 2319–2333, 2010.
- 612 Flemming, J., Benedetti, A., Inness, A., Engelen, J. R., Jones, L., Huijnen, V., Remy, S., Parrington, M., Suttie, M., Bozzo, A.,
613 Peuch, V. H., Akritidis, D., and Katragkou, E.: The CAMS interim Reanalysis of Carbon Monoxide, Ozone and Aerosol for
614 2003–2015, *Atmos. Chem. Phys.*, 17, 1945–1983, <https://doi.org/10.5194/acp-17-1945-2017>, 2017.
- 615 Foster, P., Storelvmo, T., Armour, K., Collins, W., Dufresne, J. L., Frame, D., Lunt, D. J., Mauritsen, T., Palmer, M. D.,
616 Watanabe, M., Wild, M., and Zhang, H.: The Earth’s Energy Budget, Climate Feedbacks, and Climate Sensitivity. In *Climate*
617 *Change 2021: The Physical Science Basis. Contribution of Working Group I to the Sixth Assessment Report of the*
618 *Intergovernmental Panel on Climate Change, Climate Change 2021 – The Physical Science Basis*, Cambridge University Press,
619 923–1054 pp., <https://doi.org/10.1017/9781009157896.009>, 2023.
- 620 Haywood, J. M. and Shine, K. P.: The effect of anthropogenic sulfate and soot aerosol on the clear sky planetary radiation
621 budget, *Geophys. Res. Lett.*, 22, 603–606, <https://doi.org/10.1029/95GL00075>, 1995.
- 622 Hegg, D. A., Covert, D. S., Rood, M. J., and Hobbs, P. V.: Measurements of aerosol optical properties in marine air, *J. Geophys.*
623 *Res. Atmos.*, 101, 12893–12903, <https://doi.org/10.1029/96JD00751>, 1996.
- 624 Huang, W., Saathoff, H., Shen, X., Ramisetty, R., Leisner, T., and Mohr, C.: Seasonal characteristics of organic aerosol
625 chemical composition and volatility in Stuttgart, Germany, *Atmos. Chem. Phys.*, 19, 11687–11700,
626 <https://doi.org/10.5194/ACP-19-11687-2019>, 2019.
- 627 HYSPLIT model: <https://www.ready.noaa.gov/HYSPLIT.php>. last accessed: June 2025.
- 628 IPCC: Climate Change 2021: The Physical Science Basis. Contribution of Working Group I to the Sixth Assessment Report
629 of the Intergovernmental Panel on Climate Change [Masson-Delmotte, V., P. Zhai, A. Pirani, S. L. Connors, C. Péan, S.
630 Berger, N. Caud, Y. Chen, edited by: Masson-Delmotte, V., Zhai, P., Pirani, A., Connors, S. L., Péan, C., Berger, S., Caus, N.,
631 Chen, Y., Goldfarb, L., Gomis, M. I., Huang, M., Leitzell, K., Lonnoy, E., Matthews, J. B. R., Maycock, T. K., Waterfield, T.,
632 Yelekçi, O., Yu, R., and Zhou, B., Cambridge University Press, Cambridge, United Kingdom and New York, NY, USA, 3949
633 pp., 2021.
- 634 Kahn, R. A., Andrews, E., Brock, C. A., Chin, M., Feingold, G., Gettelman, A., Levy, R. C., Murphy, D. M., Nenes, A., Pierce,
635 J. R., Popp, T., Redemann, J., Sayer, A. M., da Silva, A. M., Sogacheva, L., and Stier, P.: Reducing Aerosol Forcing
636 Uncertainty by Combining Models With Satellite and Within-The-Atmosphere Observations: A Three-Way Street, *Rev.*
637 *Geophys.*, 61, <https://doi.org/10.1029/2022RG000796>, 2023.
- 638 Kiehl, J. T. and Briegleb, B. P.: The Relative Roles of Sulfate Aerosols and Greenhouse Gases in Climate Forcing, *Science*.
639 260, 311–314, <https://doi.org/10.1126/SCIENCE.260.5106.311>, 1993.



- 640 Koop, T., Bookhold, J., Shiraiwa, M., and Pöschl, U.: Glass transition and phase state of organic compounds: dependency on
 641 molecular properties and implications for secondary organic aerosols in the atmosphere, *Phys. Chem. Chem. Phys.*, 13, 19238–
 642 19255, <https://doi.org/10.1039/C1CP22617G>, 2011.
- 643 Kristensen, T. B., Wex, H., Nekat, B., Njgaard, J. K., Van Pinxteren, D., Lowenthal, D. H., Mazzoleni, L. R., Dieckmann, K.,
 644 Bender Koch, C., Mentel, T. F., Herrmann, H., Gannet Hallar, A., Stratmann, F., and Bilde, M.: Hygroscopic growth and CCN
 645 activity of HULIS from different environments, *J. Geophys. Res. Atmos.*, 117, 22203, <https://doi.org/10.1029/2012JD018249>,
 646 2012.
- 647 Liu, J. and Li, Z.: Significant Underestimation in the Optically Based Estimation of the Aerosol First Indirect Effect Induced
 648 by the Aerosol Swelling Effect, *Geophys. Res. Lett.*, 45, 5690–5699, <https://doi.org/10.1029/2018GL077679>, 2018.
- 649 Liu, L., Kuang, Y., Zhai, M., Xue, B., He, Y., Tao, J., Luo, B., Xu, W., Tao, J., Yin, C., Li, F., Xu, H., Deng, T., Deng, X.,
 650 Tan, H., and Shao, M.: Strong light scattering of highly oxygenated organic aerosols impacts significantly on visibility
 651 degradation, *Atmos. Chem. Phys.*, 22, 7713–7726, <https://doi.org/10.5194/ACP-22-7713-2022>, 2022.
- 652 Liu, X. and Wang, J.: How important is organic aerosol hygroscopicity to aerosol indirect forcing?,
 653 <https://doi.org/10.1088/1748-9326/5/4/044010>, 2010.
- 654 Magee Scientific: User's manual for Aethalometer® Model AE33, 149, 2018.
- 655 Maskey, S., Chong, K. Y., Kim, G., Kim, J. S., Ali, A., and Park, K.: Effect of mixing structure on the hygroscopic behavior
 656 of ultrafine ammonium sulfate particles mixed with succinic acid and levoglucosan, *Particuology*, 13, 27–34,
 657 <https://doi.org/10.1016/J.PARTIC.2013.08.004>, 2014.
- 658 Mbengue, S., Zikova, N., Schwarz, J., Vodička, P., Šmejkalová, A. H., and Holoubek, I.: Mass absorption cross-section and
 659 absorption enhancement from long term black and elemental carbon measurements: A rural background station in Central
 660 Europe, *Sci. Total Environ.*, 794, 1–14, <https://doi.org/10.1016/j.scitotenv.2021.148365>, 2021.
- 661 Mitra, K., Mishra, H. R., Pei, X., and Pathak, R. K.: Secondary Organic Aerosol (SOA) from Photo-Oxidation of Toluene: I
 662 Influence of Reactive Nitrogen, Acidity and Water Vapours on Optical Properties, *Atmosphere (Basel)*, 13, 1099,
 663 <https://doi.org/10.3390/ATMOS13071099/S1>, 2022.
- 664 Müller, T., Laborde, M., Kassell, G., and Wiedensohler, A.: Design and performance of a three-wavelength LED-based total
 665 scatter and backscatter integrating nephelometer, *Atmos. Meas. Tech.*, 4, 1291–1303, [https://doi.org/10.5194/amt-4-1291-](https://doi.org/10.5194/amt-4-1291-2011)
 666 2011, 2011.
- 667 Myhre, G., Shindell, D., Bréon, F.-M., Collins, W., Fuglestad, J., Huang, J., Koch, D., Lamarque, J.-F., Lee, D., Mendoza,
 668 B., Nakajima, T., Robock, A., Stephens, T., Takemura, T., and Zhang, H.: Anthropogenic and natural radiative forcing, in:
 669 Climate Change 2013 the Physical Science Basis: Working Group I Contribution to the Fifth Assessment Report of the
 670 Intergovernmental Panel on Climate Change, vol. 9781107057, edited by: Stocker, T. F., Qin, D. G.-K. P., Tignor, M., Allen,
 671 S. K., Boschung, J., Nauels, A., Xia, Y., Bex, V., and Midgley, P. M., Cambridge University Press, Cambridge, United
 672 Kingdom and New York, NY, USA, 659–740, <https://doi.org/10.1017/CBO9781107415324.018>, 2013.
- 673 Németh, Z., Rosati, B., Ziková, N., Salma, I., Bozó, L., Dameto de España, C., Schwarz, J., Ždímal, V., and Wonaschütz, A.:
 674 Comparison of atmospheric new particle formation events in three Central European cities, *Atmos. Environ.*, 178, 191–197,
 675 <https://doi.org/10.1016/j.atmosenv.2018.01.035>, 2018.
- 676 Pandolfi, M., Alados-Arboledas, L., Alastuey, A., Andrade, M., Angelov, C., Artiñano, B., Backman, J., Baltensperger, U.,
 677 Bonasoni, P., Bukowiecki, N., Collaud Coen, M., Conil, S., Coz, E., Crenn, V., Dudoitis, V., Ealo, M., Eleftheriadis, K., Favez,



- 678 O., Fetfatzis, P., Fiebig, M., Flentje, H., Ginot, P., Gysel, M., Henzing, B., Hoffer, A., Holubova Smejkalova, A., Kalapov, I.,
679 Kalivitis, N., Kouvarakis, G., Kristensson, A., Kulmala, M., Lihavainen, H., Lunder, C., Luoma, K., Lyamani, H., Marinoni,
680 A., Mihalopoulos, N., Moerman, M., Nicolas, J., O'Dowd, C., Petäjä, T., Petit, J. E., Marc Pichon, J., Prokopciuk, N., Putaud,
681 J. P., Rodriguez, S., Sciare, J., Sellegri, K., Swietlicki, E., Titos, G., Tuch, T., Tunved, P., Ulevicius, V., Vaishya, A., Vana,
682 M., Virkkula, A., Vratolis, S., Weingartner, E., Wiedensohler, A., and Laj, P.: A European aerosol phenomenology - 6:
683 Scattering properties of atmospheric aerosol particles from 28 ACTRIS sites, *Atmos. Chem. Phys.*, 18, 7877–7911,
684 <https://doi.org/10.5194/acp-18-7877-2018>, 2018.
- 685 Perrone, M. R., Romano, S., Genga, A., and Paladini, F.: Integration of optical and chemical parameters to improve the
686 particulate matter characterization, *Atmos. Res.*, 205, 93–106, <https://doi.org/10.1016/j.atmosres.2018.02.015>, 2018.
- 687 Pilat, M. J. and Charlson, R. J.: Theoretical and optical studies of humidity effects on the size distribution of a hygroscopic
688 aerosol, *J. Rech. atmosphériques*, 165–170, 1966.
- 689 Ray, A., Bhowmik, M., Hazra, A., and Pandithurai, G.: The influence of aerosol hygroscopicity on clouds and precipitation
690 over Western Ghats, India, *Q. J. R. Meteorol. Soc.*, 150, 1473–1488, <https://doi.org/10.1002/QJ.4654>, 2024.
- 691 Ren, R., Li, Z., Yan, P., Wang, Y., Wu, H., Cribb, M., Wang, W., Jin, X., Li, Y., and Zhang, D.: Measurement report: The
692 effect of aerosol chemical composition on light scattering due to the hygroscopic swelling effect, *Atmos. Chem. Phys.*, 21,
693 9977–9994, <https://doi.org/10.5194/acp-21-9977-2021>, 2021.
- 694 Seinfeld, J. H. and Pandis, S. N.: *Atmospheric chemistry and physics*, Second Edi., John Wiley & Sons, Ltd, New Jersey, 1203
695 pp., https://doi.org/10.1007/978-3-662-04540-4_16, 2006.
- 696 Shen, Y., Zhi, G., Zhang, Y., Jin, W., Kong, Y., Li, Z., and Zhang, H.: An investigative review of the expanded capabilities of
697 thermal/optical techniques for measuring carbonaceous aerosols and beyond, *Environ. Pollut.*, 364, 125363,
698 <https://doi.org/10.1016/J.ENVPOL.2024.125363>, 2025.
- 699 Smith, L. I.: *A tutorial on Principal Components Analysis*, Department of Computer Science, University of Otago, University
700 of Otago, 9926479584201892 pp., 2002.
- 701 Song, M., Liu, P. F., Hanna, S. J., Zaveri, R. A., Potter, K., You, Y., Martin, S. T., and Bertram, A. K.: Relative humidity-
702 dependent viscosity of secondary organic material from toluene photo-oxidation and possible implications for organic
703 particulate matter over megacities, *Atmos. Chem. Phys.*, 16, 8817–8830, <https://doi.org/10.5194/ACP-16-8817-2016>, 2016.
- 704 Stein, A. F., Draxler, R. R., Rolph, G. D., Stunder, B. J. B., Cohen, M. D., and Ngan, F.: NOAA's HYSPLIT atmospheric
705 transport and dispersion modeling system, *Bull. Am. Meteorol. Soc.*, 96, 2059–2077, <https://doi.org/10.1175/BAMS-D-14-00110.1>, 2015.
- 707 Suchánková, L., Crumeyrolle, S., Bourriane, E., Prokeš, R., Holoubek, I., Ždímal, V., and Chiapello, I.: An insight into recent
708 PM₁ aerosol light scattering properties and particle number concentration variabilities at the suburban site ATOLL in Northern
709 France, *Sci. Total Environ.*, 959, 178190, <https://doi.org/10.1016/J.SCITOTENV.2024.178190>, 2025.
- 710 Tang, J., Li, J., Mo, Y., Safaei Khorram, M., Chen, Y., Tang, J., Zhang, Y., Song, J., and Zhang, G.: Light absorption and
711 emissions inventory of humic-like substances from simulated rainforest biomass burning in Southeast Asia, *Environ. Pollut.*,
712 262, <https://doi.org/10.1016/J.ENVPOL.2020.114266>, 2020.
- 713 Thomsen, D., Iversen, E. M., Skønager, J. T., Luo, Y., Li, L., Roldin, P., Priestley, M., Pedersen, H. B., Hallquist, M., Ehn,
714 M., Bilde, M., and Glasius, M.: The effect of temperature and relative humidity on secondary organic aerosol formation from
715 ozonolysis of Δ^3 -carene, *Environ. Sci. Atmos.*, 4, 88–103, <https://doi.org/10.1039/D3EA00128H>, 2024.



- 716 Titos, G., Lyamani, H., Cazorla, A., Sorribas, M., Foyo-Moreno, I., Wiedensohler, A., and Alados-Arboledas, L.: Study of the
717 relative humidity dependence of aerosol light-scattering in southern Spain, *Tellus B Chem. Phys. Meteorol.*, 66, 24536,
718 <https://doi.org/10.3402/tellusb.v66.24536>, 2014.
- 719 Titos, G., Cazorla, A., Zieger, P., Andrews, E., Lyamani, H., Granados-Muñoz, M. J., Olmo, F. J., and Alados-Arboledas, L.:
720 Effect of hygroscopic growth on the aerosol light-scattering coefficient: A review of measurements, techniques and error
721 sources, *Atmos. Environ.*, 141, 494–507, <https://doi.org/10.1016/j.atmosenv.2016.07.021>, 2016.
- 722 Titos, G., Burgos, M. A., Zieger, P., Alados-Arboledas, L., Baltensperger, U., Jefferson, A., Sherman, J., Weingartner, E.,
723 Henzing, B., Luoma, K., O'Dowd, C., Wiedensohler, A., and Andrews, E.: A global study of hygroscopicity-driven light-
724 scattering enhancement in the context of other in situ aerosol optical properties, *Atmos. Chem. Phys.*, 21, 13031–13050,
725 <https://doi.org/10.5194/acp-21-13031-2021>, 2021.
- 726 Toll, V., Christensen, M., Quaas, J., and Bellouin, N.: Weak average liquid-cloud-water response to anthropogenic aerosols,
727 *Nat.* 2019 5727767, 572, 51–55, <https://doi.org/10.1038/s41586-019-1423-9>, 2019.
- 728 Vodička, P., Schwarz, J., and Ždímal, V.: Analysis of one year's OC/EC data at a Prague suburban site with 2-h time resolution,
729 *Atmos. Environ.*, 77, 865–872, <https://doi.org/10.1016/j.atmosenv.2013.06.013>, 2013.
- 730 Vodička, P., Schwarz, J., Cusack, M., and Ždímal, V.: Detailed comparison of OC/EC aerosol at an urban and a rural Czech
731 background site during summer and winter, *Sci. Total Environ.*, 518–519, 424–433,
732 <https://doi.org/10.1016/j.scitotenv.2015.03.029>, 2015.
- 733 Watson-Parris, D. and Smith, C. J.: Large uncertainty in future warming due to aerosol forcing, *Nat. Clim. Chang.* 2022 1212,
734 12, 1111–1113, <https://doi.org/10.1038/s41558-022-01516-0>, 2022.
- 735 Williams, A. I. L., Stier, P., Dagan, G., and Watson-Parris, D.: Strong control of effective radiative forcing by the spatial
736 pattern of absorbing aerosol, *Nat. Clim. Chang.* 2022 128, 12, 735–742, <https://doi.org/10.1038/s41558-022-01415-4>, 2022.
- 737 Wiscombe, W. J. and Grams, G. W.: Backscattered fraction in two-stream approximations, *J. Atmos. Sci.*, 33, 2440–2451,
738 [https://doi.org/10.1175/1520-0469\(1976\)033<2440:tbfits>2.0.co;2](https://doi.org/10.1175/1520-0469(1976)033<2440:tbfits>2.0.co;2), 1976.
- 739 WMO/GAW: WMO/GAW Aerosol Measurement Procedures, Guidelines and Recommendations (2nd Edition) | Climate &
740 Clean Air Coalition, Geneva, 103 pp., 2016.
- 741 Zelinka, M. D., Smith, C. J., Qin, Y., and Taylor, K. E.: Comparison of methods to estimate aerosol effective radiative forcings
742 in climate models, *Atmos. Chem. Phys.*, 23, 8879–8898, <https://doi.org/10.5194/ACP-23-8879-2023>, 2023.
- 743 Zhang, J., Chen, Y. S., Gryspeerdt, E., Yamaguchi, T., and Feingold, G.: Radiative forcing from the 2020 shipping fuel
744 regulation is large but hard to detect, *Commun. Earth Environ.* 2025 61, 6, 1–11, <https://doi.org/10.1038/s43247-024-01911-9>,
745 9, 2025.
- 746 Zieger, P., Fierz-Schmidhauser, R., Poulain, L., Müller, T., Birmili, W., Spindler, G., Wiedensohler, A., Baltensperger, U.,
747 and Weingartner, E.: Influence of water uptake on the aerosol particle light scattering coefficients of the Central European
748 aerosol, *Tellus B Chem. Phys. Meteorol.*, 66, <https://doi.org/10.3402/TELLUSB.V66.22716>, 2014.
- 749 Zieger, P., Aalto, P. P., Aaltonen, V., Äijälä, M., Backman, J., Hong, J., Komppula, M., Krejci, R., Laborde, M., Lampilahti,
750 J., De Leeuw, G., Pfüller, A., Rosati, B., Tesche, M., Tunved, P., Väänänen, R., and Petäjä, T.: Low hygroscopic scattering
751 enhancement of boreal aerosol and the implications for a columnar optical closure study, *Atmos. Chem. Phys.*, 15, 7247–7267,
752 <https://doi.org/10.5194/acp-15-7247-2015>, 2015.